

Silicon-organic hybrid phase shifter based on a slot waveguide with a liquid-crystal cladding

Joerg Pfeifle,^{1,2} Luca Alloatti,¹ Wolfgang Freude,^{1,2} Juerg Leuthold,^{1,2} and Christian Koos,^{1,2,*}

¹Institute of Photonics and Quantum Electronics (IPQ), Karlsruhe Institute of Technology (KIT), Germany

²Institute of Microstructure Technology (IMT), Karlsruhe Institute of Technology (KIT), Germany

*christian.koos@kit.edu

Abstract: A highly efficient phase shifter based on the silicon-organic hybrid (SOH) platform is theoretically investigated and experimentally tested. The device consists of a silicon slot waveguide covered with an organic liquid-crystal (LC) cladding. A record-low voltage-length product of $U_{\pi}L = 0.085$ Vmm can be achieved for high-purity materials where an optimum operation point can be set by a DC bias. With standard materials and without a DC bias, we measure a phase shift of 35π with a drive voltage of only 5 V for a 1.7 mm long device corresponding to a voltage-length product of $U_{\pi}L = 0.24$ Vmm. The power dissipation is about six orders of magnitude smaller than that of state-of-the-art thermo-optic devices, thereby enabling dense integration of LC phase shifters in advanced photonic integrated circuits.

©2012 Optical Society of America

OCIS codes: (250.7360) Waveguide modulators; (250.5300) Photonic integrated circuits; (230.7370) Waveguides; (060.4080) Modulation.

References and links

1. S. Selvaraja, P. Jaenen, W. Bogaerts, D. Van Thourhout, P. Dumon, and R. Baets, "Fabrication of photonic wire and crystal circuits in silicon-on-insulator using 193-nm optical lithography," *J. Lightwave Technol.* **27**(18), 4076–4083 (2009).
2. M. Yang, W. M. J. Green, S. Assefa, J. Van Campenhout, B. G. Lee, C. V. Jahnes, F. E. Doany, C. L. Schow, J. A. Kash, and Y. A. Vlasov, "Non-blocking 4x4 electro-optic silicon switch for on-chip photonic networks," *Opt. Express* **19**(1), 47–54 (2011).
3. S. S. Djordjevic, L. W. Luo, S. Ibrahim, N. K. Fontaine, C. B. Poitras, B. Guan, L. Zhou, K. Okamoto, Z. Ding, M. Lipson, and S. J. B. Yoo, "Fully reconfigurable silicon photonic lattice filters with four cascaded unit cells," *IEEE Photon. Technol. Lett.* **23**(1), 42–44 (2011).
4. M. Rasras, D. Gill, M. Earnshaw, C. Doerr, J. Weiner, C. Bolle, and Y.-K. Chen, "CMOS silicon receiver integrated with Ge detector and reconfigurable optical filter," *IEEE Photon. Technol. Lett.* **22**(2), 112–114 (2010).
5. N. Walker and G. Walker, "Polarization control for coherent communications," *J. Lightwave Technol.* **8**(3), 438–458 (1990).
6. C. Doerr, P. Winzer, Y.-K. Chen, S. Chandrasekhar, M. Rasras, L. Chen, T.-Y. Liow, K.-W. Ang, and G.-Q. Lo, "Monolithic polarization and phase diversity coherent receiver in silicon," *J. Lightwave Technol.* **28**(4), 520–525 (2010).
7. D. Hillerkuss, M. Winter, M. Teschke, A. Marculescu, J. Li, G. Sigurdsson, K. Worms, S. Ben Ezra, N. Narkiss, W. Freude, and J. Leuthold, "Simple all-optical FFT scheme enabling Tbit/s real-time signal processing," *Opt. Express* **18**(9), 9324–9340 (2010).
8. L.-W. Luo, S. Ibrahim, A. Nitkowski, Z. Ding, C. B. Poitras, S. J. Ben Yoo, and M. Lipson, "High bandwidth on-chip silicon photonic interleaver," *Opt. Express* **18**(22), 23079–23087 (2010).
9. P. Dong, S. Liao, D. Feng, H. Liang, D. Zheng, R. Shafiqi, C.-C. Kung, W. Qian, G. Li, X. Zheng, A. V. Krishnamoorthy, and M. Asghari, "Low Vpp, ultralow-energy, compact, high-speed silicon electro-optic modulator," *Opt. Express* **17**(25), 22484–22490 (2009).
10. A. Liu, L. Liao, D. Rubin, J. Basak, Y. Chetrit, H. Nguyen, R. Cohen, N. Izhaky, and M. Paniccia, "Recent development in a high-speed silicon optical modulator based on reverse-biased pn diode in a silicon waveguide," *Semicond. Sci. Technol.* **23**(6), 064001 (2008).
11. W. M. Green, M. J. Rooks, L. Sekaric, and Y. A. Vlasov, "Ultra-compact, low RF power, 10 Gb/s silicon Mach-Zehnder modulator," *Opt. Express* **15**(25), 17106–17113 (2007).
12. L. Liao, A. Liu, D. Rubin, J. Basak, Y. Chetrit, H. Nguyen, R. Cohen, N. Izhaky, and M. Paniccia, "40 Gbit/s silicon optical modulator for highspeed applications," *Electron. Lett.* **43**(22), 1196–1197 (2007).

13. J. Leuthold, W. Freude, J.-M. Brosi, R. Baets, P. Dumon, I. Biaggio, M. Scimeca, F. Diederich, B. Frank, and C. Koos, "Silicon organic hybrid technology: A platform for practical nonlinear optics," *Proc. IEEE* **97**(7), 1304–1316 (2009).
14. B. Maune, R. Lawson, C. Gunn, A. Scherer, and L. Dalton, "Electrically tunable ring resonators incorporating nematic liquid crystals as cladding layers," *Appl. Phys. Lett.* **83**(23), 4689–4691 (2003).
15. W. De Cort, J. Beeckman, T. Claes, K. Neyts, and R. Baets, "Wide tuning of silicon-on-insulator ring resonators with a liquid crystal cladding," *Opt. Lett.* **36**(19), 3876–3878 (2011).
16. I.-C. Khoo, *Liquid crystals*, 2nd ed. (Wiley-Interscience, 2007).
17. L. Alloatti, J. Pfeifle, J. Mendez, W. Freude, J. Leuthold, and C. Koos, "Liquid crystal phase shifter on the SOH platform with ultra-low power consumption," in *Optical Fiber Communication Conference (OTu11.5.)*, (2012).
18. L. Alloatti, D. Korn, R. Palmer, D. Hillerkuss, J. Li, A. Barklund, R. Dinu, J. Wieland, M. Fournier, J. Fedeli, H. Yu, W. Bogaerts, P. Dumon, R. Baets, C. Koos, W. Freude, and J. Leuthold, "42.7 Gbit/s electro-optic modulator in silicon technology," *Opt. Express* **19**(12), 11841–11851 (2011).
19. R. Ding, T. Baehr-Jones, W. J. Kim, X. G. Xiong, R. Bojko, J. M. Fedeli, M. Fournier, and M. Hochberg, "Low-loss strip-loaded slot waveguides in silicon-on-insulator," *Opt. Express* **18**(24), 25061–25067 (2010).
20. V. R. Almeida, Q. Xu, C. A. Barrios, and M. Lipson, "Guiding and confining light in void nanostructure," *Opt. Lett.* **29**(11), 1209–1211 (2004).
21. H. Desmet, K. Neyts, and R. Baets, "Liquid crystal orientation on patterns etched in Silicon on Insulator," in *Integrated Optics, Silicon Photonics, and Photonic Integrated Circuits, Society of Photo-Optical Instrumentation Engineers (SPIE) Conference Series (61831Z)*, (2006).
22. CST - Computer Simulation Technology AG, *CST Microwave Studio 2012*, <http://www.cst.com> (2012).
23. C. Desimpel, J. Beeckman, H. Desmet, K. Neyts, R. James, and F. A. Fernández, "A four-electrode liquid crystal device for 2π in-plane director rotation," *J. Phys. D Appl. Phys.* **38**(21), 3976–3984 (2005).
24. W. De Cort, J. Beeckman, R. James, F. A. Fernandez, R. Baets, and K. Neyts, "Tuning silicon-on-insulator ring resonators with in-plane switching liquid crystals," *J. Opt. Soc. Am. B* **28**(1), 79–85 (2011).
25. RSoft Design Group Inc, *FemSIM 3.3 User Guide*, <http://www.rsoftdesign.com> (2011).
26. P. Mullner and R. Hainberger, "Structural optimization of silicon-on-insulator slot waveguides," *IEEE Photon. Technol. Lett.* **18**(24), 2557–2559 (2006).
27. Y.-H. Fan, Y.-H. Lin, H. Ren, S. Gauza, and S.-T. Wu, "Fast-response and scattering-free polymer network liquid crystals for infrared light modulators," *Appl. Phys. Lett.* **84**(8), 1233–1235 (2004).
28. T. Baehr-Jones, B. Penkov, J. Huang, P. Sullivan, J. Davies, J. Takayesu, J. Luo, T.-D. Kim, L. Dalton, A. Jen, M. Hochberg, and A. Scherer, "Nonlinear polymer-clad silicon slot waveguide modulator with a half wave voltage of 0.25 V," *Appl. Phys. Lett.* **92**(16), 163303 (2008).
29. P. Pagliusi, B. Zappone, G. Cipparrone, and G. Barbero, "Molecular reorientation dynamics due to direct current voltage-induced ion redistribution in undoped nematic planar cell," *J. Appl. Phys.* **96**(1), 218–223 (2004).
30. M. Kobayashi, H. Terui, M. Kawachi, and J. Noda, "2x2 optical waveguide matrix switch using nematic liquid crystal," *IEEE Trans. Microw. Theory Tech.* **30**(10), 1591–1598 (1982).
31. T. Alasaarela, D. Korn, L. Alloatti, A. Säynätjoki, A. Tervonen, R. Palmer, J. Leuthold, W. Freude, and S. Honkanen, "Reduced propagation loss in silicon strip and slot waveguides coated by atomic layer deposition," *Opt. Express* **19**(12), 11529–11538 (2011).
32. D. Donisi, B. Bellini, R. Beccherelli, R. Asquini, G. Gilardi, M. Trotta, and A. d'Alessandro, "A switchable liquid-crystal optical channel waveguide on silicon," *IEEE J. Quantum Electron.* **46**(5), 762–768 (2010).
33. G. P. Agrawal, *Fiber-Optic Communication Systems*, 4th ed. (Wiley-Interscience, 2010).
34. C. G. Poulton, C. Koos, M. Fujii, A. Pfrang, T. Schimmel, J. Leuthold, and W. Freude, "Radiation modes and roughness loss in high index-contrast waveguides," *IEEE J. Sel. Top. Quantum Electron.* **12**(6), 1306–1321 (2006).
35. H. Desmet, K. Neyts, and R. Baets, "Modeling nematic liquid crystals in the neighborhood of edges," *J. Appl. Phys.* **98**(12), 123517 (2005).

1. Introduction

Silicon-on-insulator (SOI) has become one of the most important platforms for large-scale photonic integration [1]. An impressive manifold of silicon photonic devices has been demonstrated over the last years, and the focus is currently shifting to the integration of more complex systems on a single chip. In this context, optical phase shifters are key elements for various devices and subsystems such as switches [2], tunable filters [3, 4], polarization controllers [5], advanced receivers [6], and optical signal processors [7]. Required response times range from a few microseconds for switching and tuning, over a few milliseconds for mitigating environmental influences, to a one-time compensation of fabrication tolerances. As opposed to high-speed electro-optic modulators, such phase shifters have quite relaxed specifications in terms of speed, but small device footprint, low driving voltages and ultra-low power dissipation are of prime importance.

Previous work on silicon photonic phase shifters concentrated mainly on thermo-optic devices, where resistive heaters are co-integrated with SOI waveguides, and the large thermo-

optic coefficient of silicon is exploited to induce a phase shift by locally increasing the temperature. Such devices have been widely used for, e.g., optical interleavers [8], tunable filters [4], and coherent receivers [6]. However, thermo-optic devices have typical lengths of several hundred micrometers, and they suffer from large power dissipation, thermal crosstalk and hence low integration density. Alternatively, optical phase shifts can be induced by modulating the density of free carriers in the silicon waveguide core. This can be achieved either by integrating forward-biased pin-junctions [9] or reverse-biased pn-junctions [10] into the SOI waveguide. Both approaches enable fast modulation [11, 12], but suffer from either the constant current flow and the associated power consumption in the case of forward-biased devices, or from low phase-shift efficiency and hence large device lengths if reversely biased.

These limitations can be overcome by combining SOI waveguides with organic liquid crystal claddings in a silicon-organic hybrid (SOH) approach [13–15]. Liquid crystal (LC) molecules are highly birefringent, and their orientation can be electrically controlled by external electric fields [16]. When used as a cladding material for SOI waveguides, liquid crystals enable large phase shifts at low power consumption. Previous devices used the TM mode of a strip waveguide and applied the electric field between an indium-tin-oxide (ITO) top electrode and the substrate as bottom electrode [15]. The phase shift demonstrated was as high as 14π , but a rather high drive voltage of 100 V was required, which might eventually limit the applicability of such devices.

In this work we use a novel concept for liquid crystal phase shifters based on an SOI slot waveguide. This approach combines a large overlap of the optical mode field and the liquid crystal cladding with a small separation and a fully planar configuration of the electrodes [17]. With a 1.7 mm long device and a drive voltage of only 5 V, we achieve an unprecedented total phase shift of 35π . A voltage-length product of $U_r L = 0.085$ Vmm is estimated for the optimum operation point of the device, which is to the best of our knowledge the lowest value ever demonstrated in a waveguide-based silicon device. Theoretical investigations show that the voltage-length product can be even further decreased by improved slot waveguide designs and by optimizing material properties of the LC cladding. Compared to conventional thermo-optic phase shifters the power consumption is reduced by more than six orders of magnitude.

The paper is structured as follows: In Section 2 we introduce the concept of slot-waveguide liquid crystal phase shifters. A theoretical study of the expected device performance and a systematic comparison to other LC slot- and strip-waveguide phase shifter configurations is presented in Section 3. Fabrication and experimental testing of a prototype device are explained in Sections 4 and 5. The Appendix gives mathematical details of the perturbation approach that was used for the theoretical analysis in Section 3.

2. The concept of slot-waveguide liquid crystal phase shifters

The phase shifters used in this work rely on the combination of SOI waveguides with organic liquid crystal cladding materials, Fig. 1(a). Liquid crystals typically consist of rod-like molecules that are arranged in a regular, crystal-like fashion. In the so-called nematic phase, the molecules have a long-range directional order with their long axes aligned parallel to each other, thereby forming a highly anisotropic optical material. For rod-like molecules, the local LC orientation is represented by the so-called director \mathbf{p} , a dimensionless unit vector, which is oriented parallel to the long molecular axis, Fig. 1(b). These materials exhibit uniaxial optical properties, where light polarized parallel (perpendicular) to the director experiences the so-called extraordinary (ordinary) refractive index n_e (n_o). The polarizability of the LC molecule along the long molecular axis is usually larger than in the perpendicular direction, i.e., $n_e > n_o$. By changing the orientation of the director with respect to the local electric field component of the SOI waveguide mode, we can vary the effective index and hence the optical phase at the output of the waveguide.

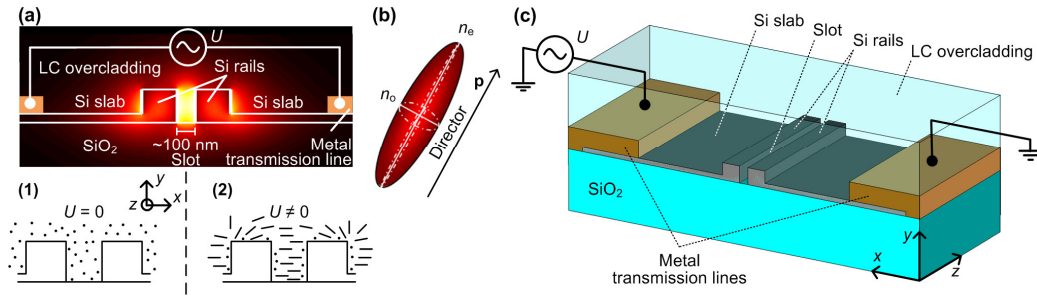


Fig. 1. Concept of the slot-waveguide liquid crystal phase shifter. (a) Cross-section of the strip-loaded slot waveguide. The silicon rails (refractive index $n = 3.48$) are connected to metal transmission lines by thin conductive silicon slabs. The waveguide is immersed in a low-index liquid crystal (LC) cladding. The orientation of the LC molecules in the slot region can be switched by the external voltage U , which drops entirely across the narrow slot and hence induces a large field strength. The color code represents the electric field magnitude of the fundamental quasi-TE mode. The high index contrast between the slot region and the silicon rails leads to strong interaction of the guided mode with the LC cladding. Insets (1) and (2): If no external voltage is applied to the slot waveguide ($U = 0$), the LC molecules align parallel to the waveguide axis (1); for nonzero voltages $U \neq 0$, the LC will partly realign along the x -direction. (b) Illustration of a rod-like LC molecule. The director \mathbf{p} represents the local direction of preferred LC orientation. Light polarized parallel (perpendicular) to the director experiences the extraordinary (ordinary) refractive index n_e (n_o). (c) Artist impression of slot waveguide. The liquid crystal covers the entire waveguide structure and completely fills the slot.

A particularly efficient electro-optical phase shifter can be realized by using a so-called strip-loaded slot waveguide [13, 18, 19]. In this configuration, the optical waveguide consists of two parallel high-index SOI rails that are spaced by a narrow slot. The silicon rails are electrically connected to metal transmission lines by thin conductive silicon slabs, Fig. 1(a) and (c). The waveguide is immersed into the low-index LC cladding. If light is coupled to the waveguide's fundamental quasi-TE mode, the dominant electric field component of the optical mode ($\underline{\mathcal{E}}_x$) will experience strong discontinuities at the rail-slot interface, leading to a field enhancement in the slot region and hence to a strong interaction of the guided light with the LC cladding [20], see mode field plot in Fig. 1(a). At the same time, an external voltage U applied to the transmission lines induces a strong field within the slot region and can be used to switch the orientation of the LC molecules.

If no external voltage is applied to the slot waveguide ($U = 0$), the LC molecules align parallel to the waveguide axis [21] and the director is oriented along the z -axis, $\mathbf{p} = \mathbf{e}_z$, where \mathbf{e}_z denotes the unit vector along the z -direction, see inset (1) in Fig. 1(a). Within the slot region, the dominant electric field component $\underline{\mathcal{E}}_x$ of the optical mode hence experiences the smaller refractive index n_o . For increasing voltages $U > 0$, the LC molecules in the slot region remote from the waveguide walls will be first to realign along the x -direction, see dashes in inset (2) of Fig. 1(a). The molecules in the vicinity of the waveguide surface tend to maintain their alignment parallel to the z -axis, indicated by dots in inset (2) of Fig. 1(a). However, for the case of very large voltages, virtually all LC molecules within the slot region are oriented along the horizontal direction, $\mathbf{p} = \mathbf{e}_x$, and the $\underline{\mathcal{E}}_x$ -component of the optical field experiences the extraordinary refractive index $n_e > n_o$. This results in a phase delay with respect to the case without external voltage.

For a given control field strength required to align the LC molecules, the associated drive voltage depends on the gap between the electrodes. It is one of the key advantages of strip-loaded slot waveguides that this gap can be made very small, and the operation voltages can hence be kept low. This is illustrated in Fig. 2, where we compare numerically calculated electric control fields of a strip-loaded slot waveguide, Fig. 2(a) and (b), and conventional slot waveguide, Fig. 2(c) and (d). To prevent optical loss, a certain minimum distance has to be

maintained between the waveguide core and the metal transmission lines. This leads to a minimum required electrode spacing of approximately $4\ \mu\text{m}$ for the case of a conventional slot waveguide, Fig. 2(c). For the strip-loaded slot waveguide, Fig. 2(a), the metal transmission lines are connected to the silicon rails by thin conductive slabs of doped silicon, such that the applied control voltage drops entirely across the narrow slot. The slot has typical widths between $100\ \text{nm}$ and $150\ \text{nm}$. The numerically calculated control field for a slot width of $120\ \text{nm}$ is depicted in Fig. 2(b) and exhibits a very homogeneous electric field distribution within the slot. For an external control voltage of $U = 1\ \text{V}$ and a slot width of $120\ \text{nm}$, we obtain a control field strength of $8\ \text{V}/\mu\text{m}$ within the slot. To achieve the same field strength in a conventional slot waveguide with remote electrodes, an external control voltage of $U = 36\ \text{V}$ is required, Fig. 2(c). Also here, the corresponding electric field in the vicinity of the waveguide core is very homogeneous, see Fig. 2(d), which is consistent with the fact that the electrode spacing is large compared to the dimensions of the waveguide core.

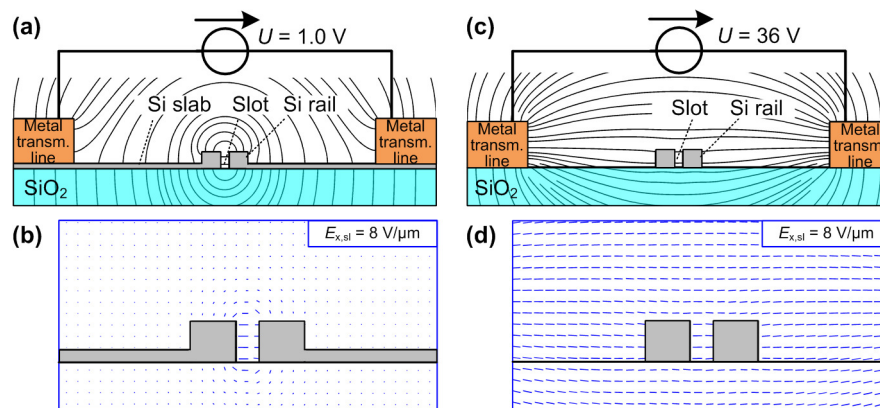


Fig. 2. Comparison of electrode configurations and electric control fields. To prevent optical loss a certain minimum distance of approximately $4\ \mu\text{m}$ has to be maintained between the metal transmission lines. (a) Strip-loaded slot waveguide: The metal transmission lines are connected to the silicon rails by thin conductive slabs of doped silicon, and the applied control voltage drops entirely across the narrow slot. For a slot of $120\ \text{nm}$ width and an external control voltage of only $U = 1\ \text{V}$, a control field strength of $8\ \text{V}/\mu\text{m}$ can be achieved within the slot. (b) Corresponding electric field in the vicinity of the waveguide core, exhibiting a homogeneous distribution in the slot region. (c) Conventional slot waveguide: Due to the large electrode spacing of $4\ \mu\text{m}$, a control voltage of $U = 36\ \text{V}$ is required to obtain an electric control field of approximately $8\ \text{V}/\mu\text{m}$ in the slot region. (d) Numerically calculated control field, exhibiting a homogeneous distribution in the vicinity of the waveguide core. For the numerical calculations of the control fields, the rail and slot widths are $240\ \text{nm}$ and $120\ \text{nm}$, respectively, and the thickness of the metal is $600\ \text{nm}$. For the strip-loaded slab waveguide, the height of the Si slab is $60\ \text{nm}$, and a conductivity of $182\ (\Omega\ \text{cm})^{-1}$ is assumed for the Si slabs and rails. Note that in (a) and (c) the numerically calculated field lines just illustrate the direction of the local control field; the density of the field lines does not correspond to the field strength. In (b) and (d) the field is represented by line elements, the length of which is proportional to the local field strength.

The numerical calculations were performed using a commercially available finite-element field simulator [22]. Field plots are derived from the eigenmode of the electrical transmission line in the low-frequency limit. For the numerical calculations of the control fields, we used a rail width and slot width of $240\ \text{nm}$ and $120\ \text{nm}$, respectively, and metal transmission lines were $600\ \text{nm}$ thick. For the strip-loaded slot waveguide, the height of the Si slab is $60\ \text{nm}$, and a conductivity of $182\ (\Omega\ \text{cm})^{-1}$ is assumed for the Si slabs and rails.

3. Numerical investigation of LC phase shifters with slot and strip waveguides

A key parameter of optical phase shifters is the achievable phase change $\Delta\phi$ per waveguide length L . For the SOH devices investigated here, this figure depends strongly on the cross-sectional geometry of the SOI waveguide core and on the optical properties of the LC

cladding. In our analysis we assume a complex propagator of the form $\exp(-j\beta z)$, where the real part β of the complex propagation constant $\underline{\beta}$ is related to the effective refractive index n_{eff} by $\beta = n_{\text{eff}} \omega / c$, and where the phase ϕ is defined as the phase angle of the complex transfer function, $\phi = -\beta z$. A voltage applied to the LC-clad slot waveguide leads to an increase of the effective index n_{eff} and hence changes the phase ϕ to more negative values.

The two most prominent examples for nematic liquid crystals with low optical loss in the infrared telecommunication wavelength range are E7 [15, 23] and CB5 [23, 24]. Both LC are in the nematic phase at room temperature. Their ordinary refractive indices as well as their extraordinary refractive indices are similar. In the following analysis we estimate the achievable phase shifts $\Delta\phi_{\text{CB5}}$ using the data of CB5 [24], i.e., $n_{\text{o, CB5}} = 1.53$, $n_{\text{e, CB5}} = 1.71$ and $\Delta n_{\text{CB5}} = n_{\text{e, CB5}} - n_{\text{o, CB5}} = 0.18$. For other materials with different values of Δn , the achievable phase shift $\Delta\phi$ can be estimated by rescaling,

$$\Delta\phi = \frac{\Delta n}{\Delta n_{\text{CB5}}} \Delta\phi_{\text{CB5}}. \quad (1)$$

This relation is based on a first-order approximation where the relative index difference is assumed to be small, i.e., $\Delta n_{\text{CB5}} \ll n_{\text{o, CB5}}$, see Appendix for a more detailed derivation.

To investigate the influence of the waveguide structure, we calculate $\Delta\phi_{\text{CB5}} / L$ for different configurations of optical waveguides and electrodes, Fig. 3(a). In our analysis, the optical properties of the cladding are represented by a permittivity tensor which depends on the orientation of the LC molecules. The phase changes are then obtained from a first-order perturbation model, in which the anisotropy of the dielectric tensor is treated as a small perturbation of an otherwise isotropic dielectric profile. The mathematical details of this method can be found in the Appendix. We use a commercially available finite-element mode solver [25] to calculate the vectorial mode fields of the isotropic waveguide. The influence of the anisotropy is finally obtained by an overlap integral of the mode fields and the perturbation tensor, Eq. (19).

The investigated waveguide configurations are depicted in Fig. 3(a), insets (1) – (6). In addition to the strip-loaded slot waveguide, Fig. 3(a), configuration (1), we investigate a conventional SOI slot waveguide with remotely located metal electrodes, Fig. 3(a), configuration (2), and strip waveguides operated in TE or TM polarization, also with distant metal electrodes that are used to apply external electric fields in the horizontal or vertical direction, Fig. 3(a), configurations (3) – (6). For all devices, we assume a height of $h = 220$ nm for the Si device layer, which represents the current standard for most SOI integration platforms. In addition, we make use of simplified models for the externally applied control fields to calculate the maximum achievable phase shift: For the strip-loaded slot waveguide, the numerical investigation of the electric control field exhibits a homogeneous field distribution in the slot region, where most of the light propagates, see Fig. 2(b). Hence, instead of accounting for the real electrode configuration, we consider a model structure, in which a homogeneous electric control field is applied via remote infinitely extended parallel-plate-like electrodes adjacent to the waveguide structures in positive and negative x -direction, Inset (1) of Fig. 3(a). Likewise, in the vicinity of a sub- μm waveguide core the control field generated by remotely located metal electrodes can be well approximated by a homogeneous electric field, see Fig. 2(d). Depending on the relative orientation of the waveguide core and the metal transmission lines, we may hence again assume a simplified model structure comprising infinitely extended parallel-plate-like electrodes adjacent to the waveguide structures in x - or y -direction, that lead to homogeneous electric control field in the LC cladding near the waveguide core, Insets (2) to (6) in Fig. 3(a).

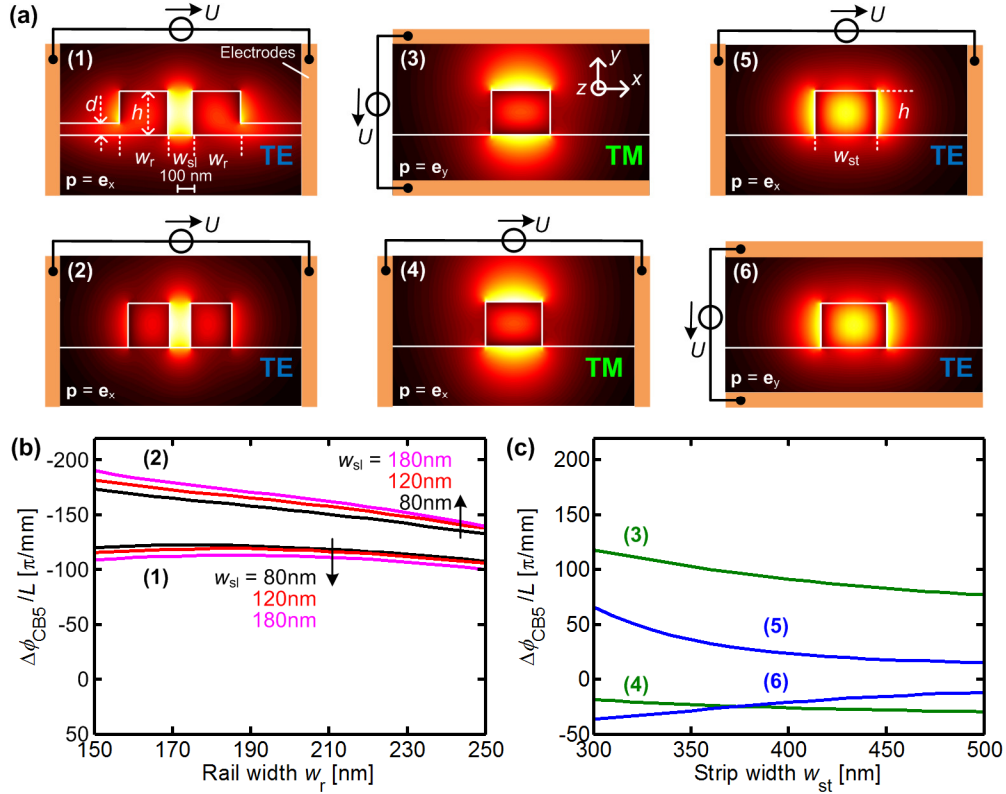


Fig. 3. Comparison of different slot- and strip-waveguide LC phase shifter designs. (a) Cross-sectional geometry and mode fields of the investigated waveguide structure: (1) Strip-loaded slot waveguide and (2) conventional slot waveguide with remotely located metal electrodes; (3) – (6) strip waveguides operated in different polarizations with remotely located metal electrodes that induce a homogeneous electric control field in the horizontal or vertical direction. (b) Computed data for the achievable phase shift $\Delta\phi_{\text{CB5}}$ per length L (negative values plotted above $\Delta\phi_{\text{CB5}} = 0$) for a strip-loaded (1) and a conventional (2) slot waveguide with various slot and rail widths w_{sl} and w_{r} . The thickness of the slab region is kept constant at $d = 60$ nm. (c) Corresponding data (negative values plotted above $\Delta\phi_{\text{CB5}} = 0$) for strip waveguides of different widths w_{st} . For all simulations, the waveguide height amounts to $h = 220$ nm and the refractive index of the silicon waveguide core and the oxide buffer layer is assumed to be 3.48 and 1.44, respectively.

Figure 3(b) shows the computed phase shifts for slot waveguides with different slot widths w_{sl} as a function of rail width w_{r} . Since we are interested in the highest achievable phase shift for a given geometry, we compare the voltage-dependent propagation constants $\beta(U)$ of the optical mode for two distinct cases: If no external voltage is applied ($U = 0$), the director is oriented along the waveguide, $\mathbf{p} = \mathbf{e}_z$, and the propagation constant of the TE mode is minimal. For very high external voltages, the director is entirely aligned along the lines of the electric control field, parallel to the x -direction, $\mathbf{p} = \mathbf{e}_x$. As a consequence, β assumes its maximum value and the phase shift saturates. The achievable phase shift for the CB5-cladding is obtained by taking the difference of these two extrema, $\Delta\phi_{\text{CB5}} = \phi(U \rightarrow \infty) - \phi(U = 0)$. This leads to the relation

$$\frac{\Delta\phi_{\text{CB5}}}{L} = \beta(U = 0) - \beta(U \rightarrow \infty). \quad (2)$$

Length-related phase shifts with magnitudes larger than $100\pi/\text{mm}$ can be achieved with slot waveguide structures, Fig. 3(b). For these structures, the propagation constant increases once

the control field is applied, and the resulting phase shift is negative. For the strip-loaded slot waveguide, configuration (1), a certain portion of the mode field propagates within the silicon slab regions adjacent to the rails. This decreases the field overlap with the LC cladding and hence leads to a smaller magnitude of the phase shift as compared to the conventional slot waveguide, configuration (2). For the conventional slot waveguide, both changes, increasing the slot width w_{sl} and decreasing the rail width w_r , lead to an increase of the modal overlap with the cladding and hence to a larger magnitude of the phase shift. In contrast to that, the phase shift obtained for the strip-loaded slot waveguide configuration (1) depends only weakly on w_r , and for the investigated configurations its magnitude even decreases if w_{sl} is increased. This can be explained by the influence of the slab regions: If the rail width is decreased, the mode field will further extend into the cladding, but at the same time it is partially drawn into the adjacent silicon slabs. The two effects compensate each other, resulting in a weak residual w_r -dependence of the mode overlap with the cladding region. Likewise, if the slot width is increased, the mode field will show a stronger overlap with the slab regions, resulting in a net decrease of the interaction with the cladding and hence to a net decrease of the achievable phase shift magnitudes.

Note that Fig. 3(b) only shows results for the TE polarization, in which the dominant electric field component is perpendicular to the slot sidewalls and hence experiences a field enhancement in the low-index slot region [20]. This is a special feature of the TE-mode; the TM-mode of the same waveguide structure does not experience this effect. The phase shift would hence be much smaller, or the mode would not even be guided. Slot waveguides can in principle also be designed for TM polarization by incorporating a horizontal instead of a vertical slot [26]. The results depicted in Fig. 3(b) can then be transferred accordingly. However the fabrication of LC-clad horizontal slot waveguides is technically challenging and does not allow for planar electrode configurations.

As a benchmark for the slot waveguides, the achievable phase shifts for different strip waveguides are calculated as a function of strip width w_{st} , Fig. 3(c). Large length-related phase shift magnitudes exceeding $100 \pi/\text{mm}$ can also be obtained for a strip waveguide operated in TM polarization in combination with an electric control field oriented along the vertical direction, configuration (3). In this structure, the electric mode field in the cladding region is predominantly oriented along the y -direction, and the external voltage switches the LC director from $\mathbf{p} = \mathbf{e}_z$ to $\mathbf{p} = \mathbf{e}_y$, resulting in an increase of the effective index and hence in a negative value of $\Delta\phi$. If the width w_{st} of the silicon strip is decreased, the overlap of the waveguide mode with the top cladding and hence the phase shift magnitude increases. A waveguide according to configuration (3) was, e.g., used for the experiments reported in Ref [15]. Combining a TM-operated strip waveguide with an electrode configuration that induces an electric control field along the x -direction, configuration (4), results in a phase shift of positive sign and considerably reduced magnitude: For zero control voltage, we have $\mathbf{p} = \mathbf{e}_z$, and the z -component of the electric mode field in the cladding region interacts with the long axis of the LC molecules. Since for a TM-mode the x -component of the electric mode field is smaller than its z -component, the effective index decreases once the control field rotates the long axis of the LC molecules from the z - to the x -direction, $\mathbf{p} = \mathbf{e}_x$. This results in a reduction of the phase delay and hence a positive value of $\Delta\phi$. In contrast to that, if a narrow TE-operated strip waveguide and an external electric field oriented along the x -direction are used, negative phase shifts with a magnitude of more than 60π can be achieved per millimeter, configuration (5). Decreasing the waveguide width further would result in even higher phase shifts, but the optical mode is then only weakly guided and tends to leak into the silicon substrate. For TE polarization in combination with vertically oriented electric control fields, the phase shift is again much weaker and of positive sign, configuration (6).

These results already show the advantages of slot waveguide configurations as opposed to strip waveguides. We have used simplified models for the electrode configurations which assume remotely located metal electrodes that lead to homogeneous electric control fields in the vicinity of the waveguide core. These models allow to predict the maximum achievable

phase shift $\Delta\phi_{\text{CB5}}/L$ for large control voltages $U \rightarrow \infty$, but cannot account for the actual electrode spacing and do hence not allow to predict the voltage-dependent phase shift. For the strip-loaded slot waveguide, Fig. 3(b) (1), the metal electrodes are connected to the conductive Si slab regions (thickness d) such that the applied control voltage drops entirely across the narrow slot. The slot has typical widths of the order of 100 nm, whereas all other configurations must have electrode separations of at least a few micrometers to avoid losses by optical absorption in the metal. For a given control field strength in the slot region, this leads to a significant decrease of the external control voltage for the case of the strip-loaded slot waveguide, see Fig. 2. Hence, the voltage-length product $U_{\pi}L$ of the strip-loaded slot waveguide is expected to be at least an order of magnitude smaller than that of the other structures depicted in Fig. 3, even though the conventional slot waveguide would allow for slightly larger length-related phase shifts $\Delta\phi/L$. Therefore, the remainder of the paper concentrates on an experimental investigation of the strip-loaded slot waveguide.

4. Device fabrication

Strip-loaded slot waveguide prototypes were produced by 193 nm deep-UV lithography and dry etching. Figure 4(a) depicts an SEM image of the device cross section. The device layer is doped with arsenic such that the silicon slabs exhibit a uniform donor concentration of 10^{17} cm^{-3} . A similar structure has been previously used for an SOH high-speed electro-optic modulator [18]. The waveguides have a height of $h = 220 \text{ nm}$ and are optically isolated from the substrate by a $2 \mu\text{m}$ thick buried oxide. The width of the silicon rails is $w_r = 240 \text{ nm}$, and they are separated by a slot with a width of $w_{\text{sl}} \approx 120 \text{ nm}$. The slab regions adjacent to the silicon rails have a thickness of $d = 60 \text{ nm}$ and are connected to metal transmission line electrodes. During fabrication, the slot was accidentally etched $1 \mu\text{m}$ deep into the buried oxide, and the separation of the metal transmission lines is only $2 \mu\text{m}$ rather than the initially designed $4 \mu\text{m}$. These imperfections increase optical loss but do not affect the phase-shifting performance significantly. The phase shifter region is $L = 1.7 \text{ mm}$ long and is connected to two grating couplers via strip-to-slot converters and conventional strip waveguides.

The LC used in the experiment is the nematic crystal 1-(trans-4-Hexylcyclohexyl)-4-isothiocyanatobenzene distributed by Sigma-Aldrich (linear formula $\text{CH}_3(\text{CH}_2)_5\text{C}_6\text{H}_{10}\text{C}_6\text{H}_4\text{NCS}$, product number #366854), see Fig. 4(b), which is in its nematic phase at room temperature. A small amount of the LC was drop-cast on the waveguide under normal atmosphere. The material covers the entire waveguide structures and penetrates the narrow slots as sketched in Fig. 1(c). We observe a strong phase shift once a control voltage U is applied to the transmission line, and the phase shift disappears when the voltage is turned off. These findings are consistent with the notion that the LC molecules are initially oriented parallel to the waveguide sidewalls, $\mathbf{p} = \mathbf{e}_z$, and that they re-align along the x -axis, if an external control field is applied, $\mathbf{p} = \mathbf{e}_x$. When turning off the control field, the LC molecules return to their initial orientation $\mathbf{p} = \mathbf{e}_z$.

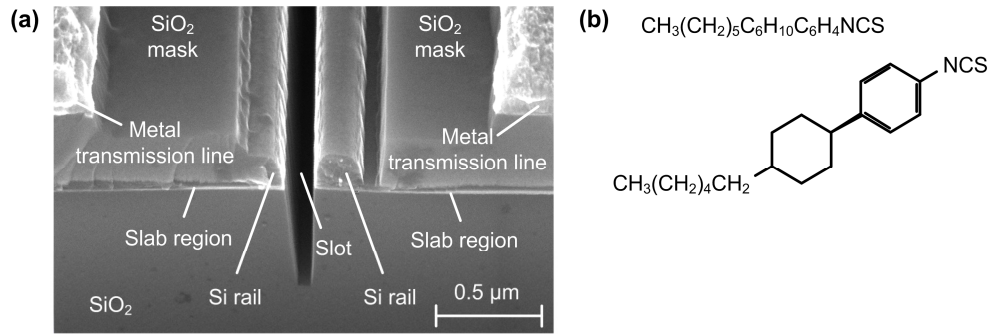


Fig. 4. Fabricated prototype phase shifter. (a) SEM picture of strip-loaded slot waveguide and metal transmission line prior to application of the LC overcladding. The SiO₂ mask was used as an etch stop layer for the metallization process. The slot was accidentally etched 1 μm deep into the buried oxide, which increases optical loss but does not affect the phase-shifting performance significantly. (b) Chemical formula and molecular structure of liquid crystal used as a cladding (Sigma-Aldrich, product #366854). The material is in its nematic phase at room temperature and covers the entire chip.

5. Experiment

For measuring the phase shift of the device, we mount it in one arm of a fiber-based Mach-Zehnder interferometer (MZI) as sketched in Fig. 5. A periodic signal is applied to the chip by micro needles. The interference pattern at the output of the MZI is recorded by a balanced photodetector PD₁ and an oscilloscope and is used to extract the phase shift during one cycle of the external voltage. The modulation speed of the applied electric field was chosen to be 100 Hz, which is high enough to separate the phase shift of the device under test from slow thermal drifts of the interferometer. On the other hand the modulation signal is slow enough such that the liquid crystal molecules can follow. The reaction time of commonly used liquid crystals in below 1 ms [27], which is fast enough for typical applications of optical phase shifters such as reconfigurable optical signal processing, mitigation of environmental influences or compensation of fabrication tolerances. The optical insertion loss is measured with a second photodetector PD₂ placed after a 3 dB directional coupler at the output of the device.

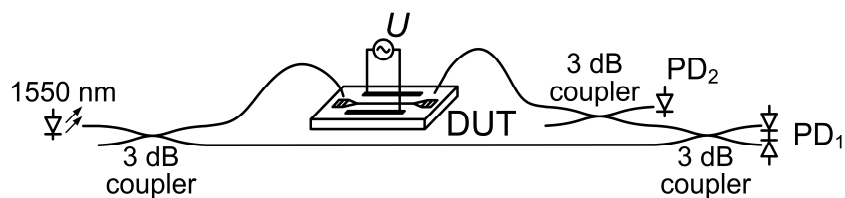


Fig. 5. Measurement setup: The phase shift of the strip-loaded slot waveguide is measured by a fiber-based Mach-Zehnder interferometer (MZI). Light from a 1550 nm laser source is split by a 3 dB directional coupler. One part is launched in the device under test (DUT) by grating couplers. At the output of the chip, the optical power is monitored by a 3 dB coupler and a photodetector (PD₂). The remaining light coming from the device interferes with light from the fiber arm of the MZI. The interference pattern is recorded with a balanced photodetector (PD₁). The phase shift is deduced from the number of fringes that occur during one cycle of the control voltage U .

In a first experiment, a zero-mean 100 Hz sawtooth signal with 5 V amplitude was applied to the device, and the phase shift was recorded as a function of time, Fig. 6(a). When the voltage crosses the zero line, the phase shift magnitude reaches a minimum. We further observe that the phase shift does not depend on the polarity of the control voltage. This can be understood from the fact that the alignment of the LC molecules along the lines of the control field is driven by induced dipole moments. If the polarity of the control field changes its sign,

the induced dipole moment is instantaneously reversed, too. The resulting torque and the alignment of the LC molecules hence remain unchanged.

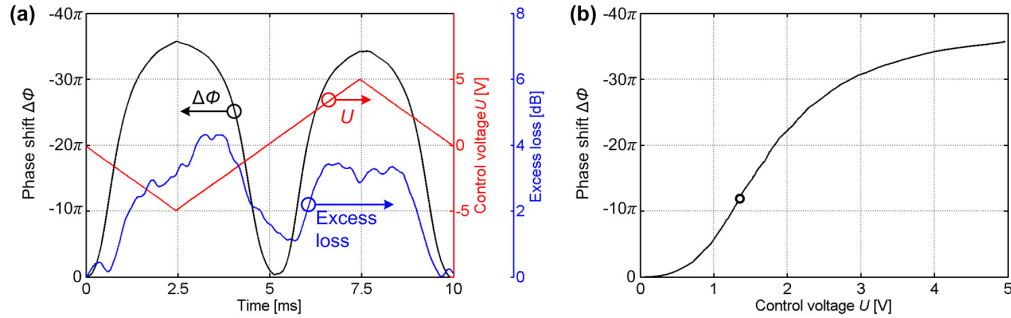


Fig. 6. Phase shift of an LC-clad slot waveguide when applying a 100 Hz sawtooth signal with 5V amplitude and without bias. (a) Time resolved measurement of the phase shift $\Delta\phi$ (black curve) induced by the control signal (red curve). Negative values of $\Delta\phi$ are again plotted above $\Delta\phi = 0$. The blue curve shows the excess insertion loss due to the variation of the liquid crystal orientation. (b) Phase shift as a function of control voltage. The phase shift magnitude saturates at approximately 35π . The highest slope $|d(\Delta\phi)/dU| = 20\pi/V$ is found at a control voltage of approximately 1.3 V; the ideal operation point is indicated by a circle. This measured slope corresponds to a voltage-length product $U_\pi L = 0.085$ Vmm for the $L = 1.7$ mm long device.

The maximum phase shift magnitude of 35π is obtained at a control voltage of ± 5 V for a 1.7 mm long device. This corresponds to a length-related phase shift of $21\pi/\text{mm}$ and a voltage-length product of $U_\pi L = 0.24$ Vmm. The optical properties of the LC cladding (Sigma-Aldrich, product #366854) at $1.55 \mu\text{m}$ wavelength are not known, but we expect that the index difference $\Delta n = n_e - n_o$ is smaller than that for CB5. Comparing the measured phase shift to the theoretically estimated value that is more than $100\pi/\text{mm}$ for the same waveguide structure and a CB5 cladding, Fig. 3(b), there is room for a 5-fold improvement of the current experimental results.

From the time-dependent measurements, we derive the phase shift $\Delta\phi$ as a function of the applied control voltage U , Fig. 6(b). This function is strongly nonlinear: For low voltages $U < 1$ V, intrinsic alignment forces must be overcome, resulting in a small slope of $|\Delta\phi|$ as a function of the applied voltage. For voltages between 1 V and 3 V, the majority of the LC molecules realigns, beginning in the bulk region of the cladding, from where the aligned domains will spread towards the core-cladding interface. This leads to a steady increase of the phase shift magnitude. For large voltages beyond 4 V, most of the molecules are already aligned along the x -direction, and the phase shift magnitude saturates. Higher voltages will only marginally increase the phase shift magnitude. The largest differential phase shift of $|d(\Delta\phi)/dU| = 20\pi/V$ is obtained at an operation point around 1.3 V, corresponding to a voltage-length product of $U_\pi L = 0.085$ Vmm. This value is — to the best of our knowledge — the lowest reported for a silicon waveguide with LC cladding [15], polymer cladding [28], or for a pn-junction [11].

In a second experiment we applied a small sawtooth-shaped modulation u_1 on top of a constant bias voltage U_0 , leading to a constant phase offset $\Delta\phi_0$ and a time-dependent phase shift $\Delta\phi_1$. For the sawtooth signal u_1 , the amplitude was chosen as high as 1 V to facilitate the analysis of the interference fringes measured by photodetector PD 1 at the output of the Mach-Zehnder interferometer, Fig. 5. The experiment was repeated at different bias voltages U_0 starting from 9V and decreasing in steps of 1V. The results for a bias of $U_0 = 7$ V are presented in Fig. 7(a). The time-dependent phase response $\Delta\phi_1$ is slightly delayed with respect to the sawtooth modulation voltage u_1 , which we attribute to the dynamics of the LC

molecule reorientation. When plotting $\Delta\phi_1$ as a function of u_1 , Fig. 7(b) we find a slightly nonlinear relationship, which is due to the rather large small-signal amplitude of 1 V together with the strongly curved large-signal characteristic, Fig. 6(b). At $u_1 = 0$ V, the slope of the curve, averaged over several measurement traces, amounts to $|\Delta\phi_1/u_1| = (12.7 \pm 0.7) \pi/V$, which corresponds to a voltage-length product of $U_\pi L = 0.13$ Vmm for the 1.7 mm long device. The averaging is done to reduce the effects of temporal phase drift caused by the fiber based Mach-Zehnder interferometer and of inaccuracies originating from the evaluation of the temporal interference patterns. In the same way we obtain the slopes and the corresponding voltage-length products for $U_0 = 9$ V and $U_0 = 8$ V, see Table 1.

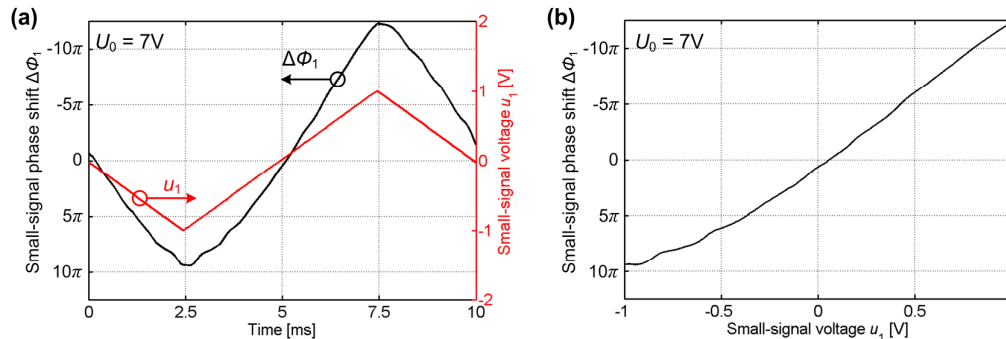


Fig. 7. Small-signal phase response $\Delta\phi_1$ of the device when applying a 100 Hz sawtooth signal u_1 with 1V amplitude on top of a DC bias of $U_0 = 8$ V. (a) Time-resolved measurement of the small-signal phase shift $\Delta\phi_1$ (black curve) induced by the time-dependent control signal u_1 (red curve). (b) Small-signal phase shift $\Delta\phi_1$ as a function of voltage u_1 . We find an approximately linear behavior with a slope of $|\Delta\phi_1/u_1| \approx 12.7 \pi/V$ at $u_1 = 0$ V. This corresponds to a voltage-length product of $U_\pi L \approx 0.13$ Vmm for the 1.7 mm long device.

Table 1. Slopes $|\Delta\phi_1/u_1|$ at $u_1 = 0$ V and Corresponding Voltage-length Products Obtained from Small-signal Measurements with Different Bias Voltages U_0

Bias U_0 [V]	$ \Delta\phi_1/u_1 $ [V^{-1}]	$U_\pi L$ [V mm]
9	$(3.9 \pm 0.3) \pi$	0.44 ± 0.03
8	$(8.0 \pm 0.6) \pi$	0.21 ± 0.02
7	$(12.7 \pm 0.7) \pi$	0.13 ± 0.01

We find that it is not possible to directly relate the small-signal measurements to the large-signal response: From the large-signal characteristics depicted in Fig. 6(b), we would expect an optimum operation point at a bias voltage of only 1.3 V, and given the 1 V amplitude of the sawtooth modulation signal, the amplitude ratio $\Delta\phi_1/u_1$ should amount to approximately $13 \pi V^{-1}$. In the small-signal measurements, however, this ratio is obtained for a much larger bias voltage of $U = 7$ V. We attribute this finding to a drift of impurity ions within the LC cladding induced by the DC component U_0 , a known effect in LC cells [16]: The spatial separation of negative and positive ions in the slot region leads to an internal electric field that partly counterbalances the externally applied bias field [29]. As a consequence, the effective internal bias voltage is smaller than the externally applied voltage U_0 , and the actual operating point on the large-signal characteristic in Fig. 6(b) shifts to the left. This effect does not play a role in the large-signal experiment, where a DC-free sawtooth signal of 100Hz was used: The complete separation of the impurity ions and the associated shielding of the electric control field build up on a time scale of seconds [29] and can therefore not follow the modulation field.

The highest voltage applied to LC devices during the experiments was 10V, and this did not cause an electrical breakthrough in the slot region. However, if a small nonzero DC bias is applied over several hours, the effects of ion separation become partially irreversible and persist even after the external bias voltage is turned off. At the beginning of the experiment we repeatedly performed measurements at bias voltages of 7 V, 8 V and 9 V, obtaining results that are comparable within the measurement accuracy. Subsequent experiments performed at bias voltage of less than 7 V, however, did not yield any conclusive interference patterns any more. We attribute this to adsorption of impurity ions to the electrodes, which leads to a permanent degradation of the device. In our setup, the LC was exposed to normal atmosphere without being protected by any cover. In future LC phase shifters, the fabrication of sealed devices with highly pure LC molecules could solve this issue. Alternatively, ion drift can be prevented by using zero-mean AC control signals with frequencies of 10 to 100 kHz [15].

In addition to the phase shifts, we observe a voltage-dependent variation of the insertion loss, see Fig. 6(a). We attribute this to the anisotropy of the imaginary part of the permittivity tensor and to light scattering occurring at the LC domain boundaries [27, 30]. However, the excess insertion loss is relatively small when compared to the achievable phase shift: For a phase shift magnitude of 35π , the loss increases by less than 4.5 dB; and a phase shifter with a 2π tuning range would therefore introduce approximately 0.25 dB of phase-dependent attenuation. For a phase shifter of known length L , this excess loss can be translated into an increase $\Delta\alpha$ of the waveguide's power attenuation coefficient. To quantify the relative magnitudes of phase delay $\Delta\phi = -\Delta\beta L$ and excess insertion loss ($4.343 \Delta\alpha L$) dB, we introduce a phase-shifter figure of merit,

$$\text{FOM}_\phi = \frac{\Delta\beta}{\Delta\alpha/2} = -2 \frac{\Delta\phi}{\Delta\alpha L} > 0. \quad (3)$$

For a device of given FOM_ϕ , a phase shift of $\Delta\phi$ leads to a change of the insertion loss by approximately $(8.69 \Delta\phi/\text{FOM}_\phi)$ dB. For our device, the 4.5 dB excess loss for a 35π phase shift correspond to a figure of merit $\text{FOM}_\phi \approx 68\pi$. We expect that a systematic study of the liquid crystals available on the market will allow to further increase this figure of merit. We aim at phase shifters with an operating range of more than 2π and less than 0.1 dB or 0.05 dB phase-dependent insertion loss, corresponding to a $\text{FOM}_\phi > 173\pi$ or $\text{FOM}_\phi > 347\pi$, respectively.

Concerning the total optical insertion loss of the devices, the high length-related phase shifts lead to considerably relaxed requirements with respect to the propagation loss of the slot waveguides. Assuming a 2 V operation voltage, a tuning range of 2π , and a voltage-length product of 0.085 Vmm, a device of 100 μm length is sufficient. The sample used in our experiment has a propagation loss of more than 17 dB/mm due to imperfect fabrication processes, Fig. 4(a), but strip-loaded slot waveguides have been demonstrated with propagation losses of less than 1 dB/mm [19], and further reductions are possible by atomic layer deposition (ALD) of thin TiO_2 films [31]. The deposition of the LC cladding led to an additional loss of 16 dB/mm in the current experiment, but we expect that we can significantly reduce this figure to below 2 dB/mm by using special materials with low infrared absorption such as CB5 or E7 [32]. In future devices, we would expect an insertion loss of less than 0.3 dB for a 100 μm long phase shifter and a 2 V operation voltage.

To estimate the power consumption of our device, we measure the resistance of the strip-loaded slot waveguide, which depends on the applied voltage, and varies between 1.7 G Ω for 1 V bias, 280 M Ω for 5 V bias, and 3 M Ω for 10 V bias. We attribute this to an anisotropic behavior of the ion mobility and hence the electrical conductivity within the LC cladding. When biasing the device at 1.3 V where the highest phase shift efficiency is found, the electrical power consumption would amount to about 1 nW. This value is more than six orders of magnitude smaller than the power consumption of thermally operated silicon phase shifters. In the current device, the metal electrodes of the device for ground and signal have an

area of 0.12 mm². We expect that by using smaller electrode surfaces and shorter devices, together with LC of higher purity grades and hence lower impurity ion density, we can reduce leakage currents and the power consumption by another order of magnitude.

6. Summary

By combining for the first time a silicon-on-insulator slot waveguide with a liquid crystal cladding, we demonstrate a total phase shift of 35π with a drive voltage of only 5 V for a 1.7 mm long device. In the optimum operation point of the device, we find a record-low voltage-length product of $U_\pi L = 0.085$ Vmm. The device combines a high overlap of the optical mode and the LC cladding, with a highly efficient planar electrode configuration. Our experiments show that phase shifters with lengths of 100 μm or less are feasible with operation voltages of a few volt and power dissipation in the nW range. Numerical investigations indicate that even higher phase shifts can be expected when using optimized waveguide geometries and liquid crystals with smaller phase-related loss, i.e., higher figures of merit FOM_ϕ . We consider the results an important step in silicon-based integrated optical phase shifters, enabling the integration of complex photonic systems with a multitude of phase shifters on a single chip.

Appendix: Modeling of strip- and slot-waveguide liquid crystal phase shifters

In this work, we consider high-index-contrast waveguides with optically anisotropic index profiles. For optical fibers and other waveguides with low refractive index contrast, the influence of an isotropic index perturbation can be described by means of a field confinement factor, which is derived from scalar approximations of the electromagnetic modes [33]. This concept cannot be applied to our waveguides. We therefore extend the formulation to include anisotropic perturbations of high-index-contrast structures, taking into account the vectorial nature of the electric and magnetic mode fields. Our model is based on a first-order approximation, in which the optical anisotropy within the LC cladding is treated as a small perturbation of an isotropic index profile. Here we give the mathematical details of this method, which is derived from the mode-coupling equations for anisotropic high-index-contrast waveguides.

A. Representation of an anisotropic permittivity profile in the waveguide cross-section

The structure of the LC-clad waveguide is described by a complex anisotropic permittivity tensor $\underline{\epsilon}_a(x, y)$, which can be decomposed into an isotropic part $\underline{\epsilon}_i(x, y)$ and a small anisotropic part $\Delta\underline{\epsilon}(x, y)$,

$$\underline{\epsilon}_a(x, y) = \underline{\epsilon}_i(x, y) + \Delta\underline{\epsilon}(x, y). \quad (4)$$

In general, the permittivity tensor elements are complex numbers, the imaginary parts of which account for material absorption or gain. For LC-clad SOI waveguides, the perturbation $\Delta\underline{\epsilon}(x, y)$ is nonzero in the anisotropic cladding region only, and the anisotropy depends on the local orientation of the LC molecules. Within a local (u, v, w) -coordinate system for which the w -direction (extraordinary refractive index $n_e > n_o$) is oriented along the local director \mathbf{p} of the liquid crystal, Fig. 8(a), the dielectric tensor can be represented by

$$\underline{\epsilon}_{a,uvw} = \epsilon_0 \begin{pmatrix} n_o^2 & 0 & 0 \\ 0 & n_o^2 & 0 \\ 0 & 0 & n_e^2 \end{pmatrix}, \quad (5)$$

where n_o and n_e are the ordinary and extraordinary (\mathbf{p} -direction) refractive indices of the liquid crystal, and $\epsilon_0 = 8.854 \times 10^{-12}$ As/(Vm) denotes the vacuum permittivity.

In the LC cladding, the refractive index of the isotropic background is chosen to represent the geometric mean of the ordinary and the extraordinary refractive index. This leads to an isotropic permittivity tensor of the form

$$\underline{\boldsymbol{\varepsilon}}_i = \varepsilon_0 \frac{n_e^2 + n_o^2}{2} \mathbf{I}, \quad (6)$$

where \mathbf{I} is the identity matrix. The anisotropic perturbation $\Delta\underline{\boldsymbol{\varepsilon}}(x, y)$ can now be expressed with respect to the (u, v, w) -coordinate system,

$$\Delta\underline{\boldsymbol{\varepsilon}}_{uvw} = \varepsilon_0 \frac{n_e^2 - n_o^2}{2} \begin{pmatrix} -1 & 0 & 0 \\ 0 & -1 & 0 \\ 0 & 0 & 1 \end{pmatrix}. \quad (7)$$

In the following, we assume the relative perturbation of the permittivity to be small, $n_e^2 - n_o^2 \ll n_o^2$, such that we can use the approximation $n_e^2 - n_o^2 \approx 2n_o \Delta n$ where $\Delta n = n_e - n_o$. To calculate the influence of the anisotropic perturbation on the waveguide mode, the representation within the local (u, v, w) -system must be transformed to the global (x, y, z) -coordinate system by multiplication with the corresponding rotation matrices. Representing the local orientation of the director by two angles $\varphi(x, y)$ and $\psi(x, y)$, Fig. 8(b), we obtain

$$\Delta\underline{\boldsymbol{\varepsilon}} = \varepsilon_0 \Delta n n_o \begin{pmatrix} -\cos 2\psi & \sin \varphi \sin 2\psi & \cos \varphi \sin 2\psi \\ \sin \varphi \sin 2\psi & -\cos^2 \varphi + \sin^2 \varphi \cos 2\psi & \sin 2\varphi \cos^2 \psi \\ \cos \varphi \sin 2\psi & \sin 2\varphi \cos^2 \psi & \cos^2 \varphi \cos 2\psi - \sin^2 \varphi \end{pmatrix} \quad (8)$$

In this relation, the spatial dependency of the perturbation $\Delta\underline{\boldsymbol{\varepsilon}}(x, y)$ and of the angles $\varphi(x, y)$, $\psi(x, y)$ was omitted for the sake of readability. Using Eq. (8), the influence of the LC orientation on the propagation constant β is calculated by a mode-coupling approach, the details of which are derived in the next section.

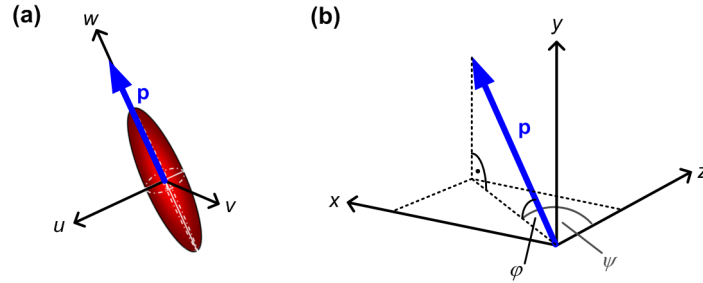


Fig. 8. Definition of coordinate systems and angles: (a) Definition of the local (u, v, w) -coordinate system that is given by the local orientation of the director \mathbf{p} such that $\mathbf{p} \parallel \mathbf{e}_w$. (b) The (x, y, z) -coordinate system is defined by the waveguide geometry as shown in Fig. 1(c). The angles φ and ψ define the orientation of the director \mathbf{p} within the (x, y, z) -coordinate system.

B. Mode expansion and perturbation ansatz

The derivation of the mode-coupling relations starts from the frequency-domain formulation of Maxwell's equations for the electric field vector $\underline{\mathbf{E}}$ and the magnetic field vector $\underline{\mathbf{H}}$,

$$\nabla \times \underline{\mathbf{E}}(x, y, z) = -j\omega\mu_0 \underline{\mathbf{H}}(x, y, z), \quad (9)$$

$$\nabla \times \mathbf{H}(x, y, z) = j\omega(\underline{\boldsymbol{\epsilon}}_i(x, y) + \Delta\underline{\boldsymbol{\epsilon}}(x, y))\mathbf{E}(x, y, z), \quad (10)$$

where $\underline{\boldsymbol{\epsilon}}_i(x, y)$ and $\Delta\underline{\boldsymbol{\epsilon}}(x, y)$ are given by Eqs. (6) and (8). Assuming a small perturbation, we approximate the electric and magnetic field by an expansion in terms of the vectorial eigenmodes $\underline{\mathcal{E}}_v(x, y)$ and $\underline{\mathcal{H}}_v(x, y)$ of the unperturbed waveguide, where z -dependent mode amplitudes $\underline{A}_v(z)$ are used as expansion coefficients,

$$\mathbf{E}(x, y, z) = \sum_v \underline{A}_v(z) \underline{\mathcal{E}}_v(x, y) \exp(-j\beta_{i,v}z), \quad (11)$$

$$\mathbf{H}(x, y, z) = \sum_v \underline{A}_v(z) \underline{\mathcal{H}}_v(x, y) \exp(-j\beta_{i,v}z). \quad (12)$$

The quantity $\beta_{i,v}$ denotes the propagation constant of the v -th mode of the isotropic waveguide. Note that in these relations, the continuum of radiation modes is approximated by a discrete set [34]. The eigenmodes of the unperturbed structure satisfy an orthogonality relation of the form

$$\frac{1}{4} \int \int_{-\infty}^{\infty} (\underline{\mathcal{E}}_v(x, y) \times \underline{\mathcal{H}}_\mu^*(x, y) + \underline{\mathcal{E}}_\mu^*(x, y) \times \underline{\mathcal{H}}_v(x, y)) \cdot \mathbf{e}_z dx dy = P_v \delta_{v\mu} \quad (13)$$

where the asterisk denotes the complex conjugate, $\delta_{v\mu}$ is Kronecker's delta and P_v represents the power that is associated with the numerically calculated mode fields $\underline{\mathcal{E}}_v(x, y)$ and $\underline{\mathcal{H}}_v(x, y)$,

$$P_v = \frac{1}{2} \int \int_{-\infty}^{\infty} \text{Re}\{\underline{\mathcal{E}}_v(x, y) \times \underline{\mathcal{H}}_v^*(x, y)\} \cdot \mathbf{e}_z dx dy \quad (14)$$

In this representation, the complex amplitudes $\underline{A}_v(z)$ are dimensionless quantities and the physical power P_v carried by the v -th mode is given by

$$P_v(z) = |\underline{A}_v(z)|^2 P_v. \quad (15)$$

We now insert the field expansion, Eqs. (11) and (12), into Maxwell's equations, Eqs. (9) and (10). In the resulting expression, we apply the identity $\nabla \times (\Phi \mathbf{F}) = \Phi(\nabla \times \mathbf{F}) + (\nabla \Phi) \times \mathbf{F}$ where $\Phi = \underline{A}_v(z) \exp(-j\beta_{i,v}z)$ represents a scalar function, and $\mathbf{F} = \underline{\mathcal{E}}_v(x, y)$ or $\mathbf{F} = \underline{\mathcal{H}}_v(x, y)$, respectively, is a vector field. The equations can be simplified by exploiting the fact that the mode fields fulfill Maxwell's Eqs. (9) and (10) for the unperturbed waveguide structure, i.e., for $\Delta\underline{\boldsymbol{\epsilon}} = 0$. We then form the scalar products of the resulting equations with the vector fields $\underline{\mathcal{H}}_\mu^*(x, y)$ and $\underline{\mathcal{E}}_\mu^*(x, y)$, respectively, subtract them and integrate over the whole (x, y) -plane. Using Eq. (13), we can project out the evolution of an individual mode amplitude $\underline{A}_\mu(z)$ during propagation along the z -direction. This leads to a set of coupled differential equations for the mode amplitudes,

$$\frac{d\underline{A}_\mu(z)}{dz} = -j \sum_v \kappa_{\mu v} \underline{A}_v(z) \exp(-j(\beta_v - \beta_\mu)z), \quad (16)$$

where the mode coupling coefficients $\kappa_{\mu\nu}$ are obtained from an overlap integral of the electric mode fields with the perturbation $\Delta\underline{\epsilon}$ of the permittivity tensor,

$$\kappa_{\mu\nu} = \frac{\omega}{2} \frac{\iint_{-\infty}^{\infty} (\Delta\underline{\epsilon}(x, y) \underline{\mathcal{E}}_{\nu}(x, y)) \cdot \underline{\mathcal{E}}_{\mu}^*(x, y) dx dy}{\iint_{-\infty}^{\infty} \text{Re}\{\underline{\mathcal{E}}_{\mu}(x, y) \times \underline{\mathcal{H}}_{\mu}^*(x, y)\} \cdot \mathbf{e}_z dx dy}. \quad (17)$$

The coupled-mode relations according to Eq. (16) can be simplified by considering axially homogenous single-mode waveguides with well-confined mode fields, where higher-order guided modes and radiation modes can be neglected. Retaining only the dominant mode amplitude $\underline{A}_{\nu}(z)$ in Eq. (16) we can rewrite the relation in the form

$$\frac{d\underline{A}_{\nu}(z)}{dz} = -j\Delta\beta_{\nu} \underline{A}_{\nu}(z), \quad (18)$$

where $\Delta\beta_{\nu}$ denotes the real part of the anisotropy-related change $\Delta\underline{\beta}_{\nu}$ of the complex propagation constant

$$\Delta\beta_{\nu} = \text{Re}\{\Delta\underline{\beta}_{\nu}\}; \quad \Delta\underline{\beta}_{\nu} = \frac{\omega}{2} \frac{\iint_{-\infty}^{\infty} (\Delta\underline{\epsilon}(x, y) \underline{\mathcal{E}}_{\nu}(x, y)) \cdot \underline{\mathcal{E}}_{\nu}^*(x, y) dx dy}{\iint_{-\infty}^{\infty} \text{Re}\{\underline{\mathcal{E}}_{\nu}(x, y) \times \underline{\mathcal{H}}_{\nu}^*(x, y)\} \cdot \mathbf{e}_z dx dy}. \quad (19)$$

The phase-shifter figure of merit FOM_{ϕ} as defined in Eq. (3) can be directly related to the real and the imaginary part of the complex quantity $\Delta\underline{\beta}_{\nu}$,

$$\text{FOM}_{\phi} = \frac{\text{Re}\{\Delta\underline{\beta}_{\nu}\}}{\text{Im}\{\Delta\underline{\beta}_{\nu}\}}. \quad (20)$$

Note that the tensor $\Delta\underline{\epsilon}(x, y)$ in the numerator of Eq. (19) is represented by a 3×3 -matrix, which is first multiplied with a 3×1 -vector $\underline{\mathcal{E}}_{\nu}$, resulting in a 3×1 -vector. After scalar multiplication with the 3×1 -vector $\underline{\mathcal{E}}_{\nu}^*$, we obtain a scalar quantity with a positive or negative real part, depending on the relative orientation of $\Delta\underline{\epsilon} \underline{\mathcal{E}}_{\nu}$ and $\underline{\mathcal{E}}_{\nu}^*$. This quantity is then integrated over the entire (x, y) -plane. The sign of the resulting phase shift hence depends on the orientation of the LC director with respect to the electric mode field, see also the results presented in Fig. 3(c) and the discussion thereof. Under the influence of the anisotropic cladding material, the ν -th mode's propagation constant β_{ν} is given by the mode propagation constant $\beta_{i,\nu}$ of the isotropic structure corrected by $\Delta\beta_{\nu}$,

$$\beta_{\nu} = \beta_{i,\nu} + \Delta\beta_{\nu}. \quad (21)$$

Inserting Eq. (8) in Eq. (19), it is found that the change $\Delta\beta_{\nu}$ of the propagation constant is proportional to the difference between the extraordinary and ordinary refractive index $\Delta n = n_e - n_o$ of the LC, leading to Eq. (1).

We tested the validity of our model by comparing the predicted changes $\Delta\beta_{\nu}$ of the propagation constant to finite-element reference simulations of waveguides with isotropic cladding materials. As an example, we consider a slot waveguide according to configuration (2) in Fig. 3(a) with a slot width of $w_{\text{sl}} = 120$ nm, rail width of $w_r = 240$ nm, and a CB5 cladding. For the fundamental TE-mode, switching the LC orientation from the z - to the x -

direction leads to an increase of the effective refractive index by $\Delta n_{\text{eff}} = 0.109$ according to our anisotropic perturbation model. When instead we approximate the LC orientation $\mathbf{p} = \mathbf{e}_x$ ($\mathbf{p} = \mathbf{e}_z$) by an isotropic cladding with a refractive index that corresponds to the ordinary index $n_{o,\text{CB5}} = 1.53$ (extraordinary index $n_{e,\text{CB5}} = 1.71$) of CB5, we obtain an effective index of $n_{\text{eff},o} = 1.844$ ($n_{\text{eff},e} = 1.985$) and hence a difference of $\Delta n_{\text{eff},oe} = 0.141$. The isotropic approximation hence leads to an index difference that is slightly larger than the value predicted by the anisotropic perturbation model. This finding is in good agreement with the fact that in the isotropic reference simulation all components of the electric field simultaneously experience the low ordinary index $n_{o,\text{CB5}} = 1.53$ or the high extraordinary index $n_{e,\text{CB5}} = 1.71$ of the cladding. In the anisotropic model, however, only one of $\underline{\mathcal{E}}_x$ - or the $\underline{\mathcal{E}}_z$ -component interacts with the high extraordinary index, whereas all other components experience the lower ordinary index. In particular, the electric mode fields of the slot waveguide feature a notable longitudinal component $\underline{\mathcal{E}}_z$ in the cladding region outside the slot. The $\underline{\mathcal{E}}_z$ -component experiences the high extraordinary index $n_{e,\text{CB5}}$ when the LC molecules are oriented along the z -direction. Switching the orientation to the x -direction increases the index for the dominant $\underline{\mathcal{E}}_x$ -component, but also diminishes the index for the $\underline{\mathcal{E}}_z$ -component. The resulting change of the effective refractive index is therefore smaller than the one obtained from the simplified approximation.

In the analysis presented in Section 3, we used Eqs. (8) and (19) to estimate the achievable phase shifts by assuming a uniform alignment of the director along one of the coordinate axes. However, the model derived here is more general and might also be used to calculate the voltage-dependence of the phase shift. In this case, the orientation of the LC director \mathbf{p} needs to be calculated as a function of the lateral coordinates x and y by taking into account the local electric control field, the waveguide geometry, and other structures that affect the local molecule alignment [35]. The space-dependent perturbation of the dielectric tensor can then be obtained from Eq. (8) and inserted in Eq. (19) to derive the voltage-dependent change of the propagation constant.

Acknowledgments

This work was supported by the European Research Council (ERC Starting Grant ‘EnTeraPIC’, number 280145), the Center for Functional Nanostructures (CFN) of the Deutsche Forschungsgemeinschaft (DFG) (project A 4.8), by the Karlsruhe Nano-Micro Facility (KNMF), by the Karlsruhe School of Optics & Photonics (KSOP), and by the European Project SOFI (number 248609). We further acknowledge support by the Open Access Publishing Fund of Karlsruhe Institute of Technology (KIT).